Elastic Instabilities Govern the Morphogenesis of the Optic Cup

Jeong-Ho Lee[®], Harold S. Park,* and Douglas P. Holmes^{®†}
Department of Mechanical Engineering, Boston University, Boston, Massachusetts 02215, USA

(Received 2 March 2021; accepted 6 August 2021; published 23 September 2021)

Because the normal operation of the eye depends on sensitive morphogenetic processes for its eventual shape, developmental flaws can lead to wide-ranging ocular defects. However, the physical processes and mechanisms governing ocular morphogenesis are not well understood. Here, using analytical theory and nonlinear shell finite-element simulations, we show, for optic vesicles experiencing matrix-constrained growth, that elastic instabilities govern the optic cup morphogenesis. By capturing the stress amplification owing to mass increase during growth, we show that the morphogenesis is driven by two elastic instabilities analogous to the snap through in spherical shells, where the second instability is sensitive to the optic cup geometry. In particular, if the optic vesicle is too slender, it will buckle and break axisymmetry, thus, preventing normal development. Our results shed light on the morphogenetic mechanisms governing the formation of a functional biological system and the role of elastic instabilities in the shape selection of soft biological structures.

DOI: 10.1103/PhysRevLett.127.138102

Eye development is a complex, multiscale morphogenetic process that couples cell growth, division, and biological signaling at cellular scales, with large deformation and shape changes. The eye organogenesis begins with formation of the optic vesicles (OVs), nearly spherical shells that undergo invagination—a process that locally reverses the curvature of tissues from convex to concave [1], to form the optic cup (OC), a cavity that eventually houses the eye. It is well established that many congenital eye disorders arise from disruptions in embryonic eye development, including anophthalmia or microphthalmia [2], aniridia [3], coloboma [4], retinal dysplasia [5], and retinal detachment [6].

In the embryonic stage of eye development, the OV bilaterally protrudes from the forebrain and contacts the surface ectoderm (SE). The OV and the SE epithelium are attached to each other through the stiff extracellular matrix (ECM) secreted by both SE and OV, which thickens to form the lens placode and retinal placode. These placodes invaginate, such that curvature of the inner portion of the OV (IOV) changes sign compared to its outer portion (OOV) as shown in Fig. 1(a), to form the lens vesicle and OC, respectively [7,8]. Despite recent efforts [9,10], important questions remain open as to what mechanisms govern OC morphogenesis during and after invagination [5,11–17] and how growth of the IOV and OOV, and evolution of their mechanical properties, impact the morphogenetic processes.

In this Letter, we advance two novel points that contribute to the physics of OC morphogenesis. First, the morphogenetic process is driven by two elastic instabilities that are analogous to snap-through instabilities in spherical shells. These occur at different times during OC

development, corresponding to invagination and rapid deepening observed in biological experiments [13,18]. Second, we demonstrate that the second morphogenetic instability is sensitive to OC geometry. Specifically, for certain geometries, the OC buckles rather than snaps during the second instability, which breaks axisymmetry, and prevents normal OC morphogenesis. This result suggests that some congenital eye disorders, such as glaucoma in newborn infants [19], may be due to OC geometry during morphogenesis.

The OV geometry motivates a simplification of their initial shape to a spherical shell. The ECM and IOV form a

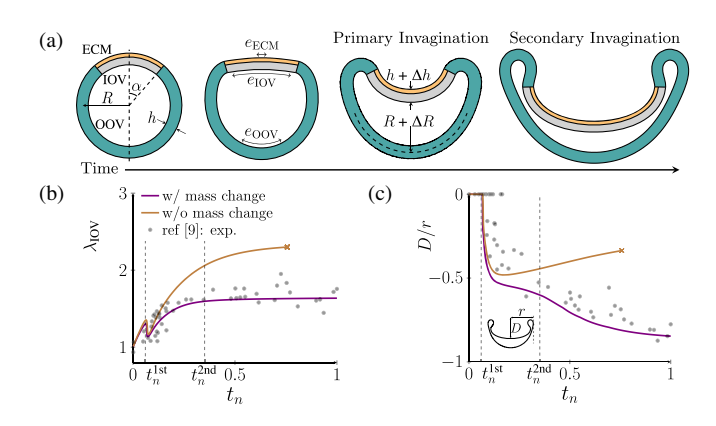


FIG. 1. (a) Simplified schematic of the OC morphogenesis. (b) Thickness change ratio of IOV center wall $\lambda_{\rm IOV}$ as function of the normalized time t_n . (c) Invagination depth D normalized by OC horizontal radius r as function of t_n . (b) and (c) show comparisons of our model with existing experimental data [9], using R/h = 5 and $\alpha = 40^\circ$ with primary and secondary invagination at $t_n^{\rm 1st}$ and $t_n^{\rm 2nd}$.

bilayer cap that subtends an opening angle α , while the OOV is a monolayer covering the rest of the sphere [Fig. 1(a)]. We modeled the mechanical response of the OC as a multilayer Kirchhoff-Love (KL) shell [20], which assumes the 3D shell may be represented by its 2D midsurface. Each layer of the KL shell (ECM, IOV, and OOV) is, in contrast to recent works using shells to study biological morphogenesis [29-31], allowed to undergo large strains and rotations and change thickness, via the plane-stress condition, during deformation while being modeled by a compressible neo-Hookean material model [32,33], which takes the energy density form $\Psi_0 = (\lambda/4)(J_m^2 - 1 - 2\log J_m) + (\mu/2)(I_{m1} - 3 - 2\log J_m)$ with Lamé constants λ and μ , and invariants I_{m1} and J_m of the elastic right Cauchy-Green tensor. To account for large strains and rotations during growth, we utilize the wellestablished multiplicative decomposition of deformation gradient F into growth F_q and elastic deformation F_m parts [34-37]. Each layer of the OC is subject to isotropic area growth via $F_a = (e, e, 1)$ where e is the in-plane expansion factor due to growth [20]. We simulate the OC formation process by solving two coupled balance equations: linear momentum balance to determine elastic deformation via F_m and mass balance to account for growth via F_q . These equations are solved numerically using the isogeometric analysis method, a modern finite-element-like method that is well suited for shell problems due to its ability to provide an accurate shell midsurface description [38].

We model the differential growth during OC formation by imposing different mass sources on the ECM, IOV, and OOV in the manner of density-preserving growth [9], such that the three regions have different (experimentally measured) growth rates [9], i.e., $e_{\rm ECM}(t_n)=1, \ e_{\rm IOV}(t_n)=1+5t_n$, and $e_{\rm OOV}(t_n)=1+1.5t_n$ as a function of the normalized time $t_n=t/\tau$, where $\tau=20$ hours is the experimentally measured timescale for OC morphogenesis. The fluidlike components surrounding the OV are neglected [39–41], based on previous studies showing that instabilities of spherical shells are not suppressed by the surrounding fluid environment [42].

A critical, but often neglected, feature in morphogenetic modeling is the effect that mass addition during growth has on the state of stress of the growing body. We find that [see Supplemental Material (SM) for detailed derivation [20]], if the added material during density-preserving growth is the same as the existing material in the body, the stress Σ^{ij} generated in the growing body is amplified as

$$\Sigma^{ij} = e^2 \frac{\partial \Psi_0}{\partial \epsilon_{ij}},\tag{1}$$

where Ψ_0 is the neo-Hookean strain energy density, and ϵ_{ij} is the strain tensor. Thus, e^2 acts as a stress amplification

factor on the internal stress due to mass change from growth, in which $\partial \Psi_0/\partial \epsilon_{ij}$ is the standard representation for the internal stress [43]. This stress amplification factor e^2 generalizes previous works [44], as shown in the SM [20].

First, we show that our computational model can capture existing experimental data for OC morphogenesis in a chick embryo [9,10], as shown in Figs. 1(b) and 1(c). The geometric and material parameters for the chick OVs followed previous experiments [9,10,45], i.e., opening angle $\alpha=40^\circ$, initial radius (R) of 50 μ m, and radius to total thickness ratio (R/h) of 5. The bilayer cap has ECM thickness ($h^{\rm ECM}$) of h/10 and IOV thickness ($h^{\rm IOV}$) of 9h/10 whose ratio is $m=h^{\rm ECM}/h^{\rm IOV}=1/9$, and the monolayer OOV has thickness ($h^{\rm OOV}$) of h. The shear moduli for the ECM and the IOV and OOV are 11 kPa ($\mu^{\rm ECM}$) and 220 Pa ($\mu^{\rm IOV}$ and $\mu^{\rm OOV}$), respectively, whose ratio is $n=\mu^{\rm ECM}/\mu^{\rm IOV}=50$ on the bilayer cap. Poisson's ratio for all regions was set to $\nu=0.45$ based on biologically observed data showing that eye tissue is not incompressible [46,47].

Figures 1(b) and 1(c) show the simulation results of OC formation with and without accounting for the effect of mass change during growth on the stress, where neglecting the mass change corresponds to taking $e^2 \rightarrow 1$ in (1). By comparing to the experimental results [9], it is clear that our model accurately captures the evolution of thickness change ratio of the IOV center wall (λ_{IOV}) as well as invagination depth (D) normalized by OC horizontal radius (r), which are geometric parameters that characterize the OC size and shape. Therefore, the stress amplification from mass addition significantly impacts the local and inhomogeneous growth and enables the accurate simulation of experimentally observed OC growth. This also demonstrates that there is no need to prescribe hypothetical stiffness or growth property gradients as in previous OC growth modeling [9,10].

The OV thickness is known to vary with diverse biological cues, such as protein-2 alpha [48–50], which implies that the radius-thickness ratio R/h of initial OC shape also varies with different biological situations. To account for these unknown thickness variations, we performed numerical simulations at $\alpha=40^\circ$ with different R/h within the biologically relevant range (5 to 20) [51–53]. This initial geometry is characterized using a single, dimensionless parameter $\bar{\theta}=\alpha\sqrt{R/h}$, which describes the depth and slenderness of the bilayer cap region relative to the angular width of the boundary layer [54].

For all values of $\bar{\theta}$ examined, the shells exhibit two distinct shape–shifting events (Fig. 2). At early times, the apex of the OC inverts, resulting in the formation of a cuplike shape, which we refer to as primary invagination (Fig. 2, $i \rightarrow ii$, $I \rightarrow II$). As t_n increases, we observe a second shape-shifting event that is sensitive to the initial

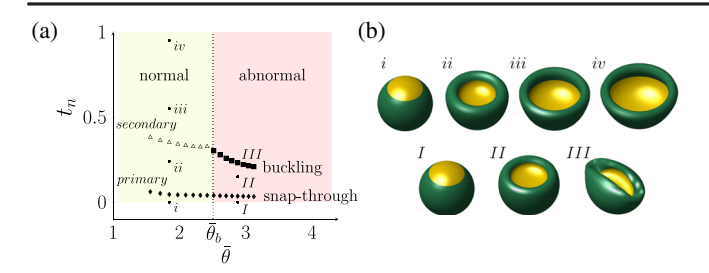


FIG. 2. (a) Simulation results varying R/h at $\alpha=40^\circ$, considering mass changes. Diamond means the first instability point while triangle and square are the second instability. At $\bar{\theta}=2.51$ ($\bar{\theta}_b$), the shape-morphing mechanism changes from secondary invagination (triangle) to buckling (square). (b) Representative OC formation process: normal OC (top row) and abnormal OC shape due to buckling (bottom row).

geometry. For lower $\bar{\theta}$, i.e., thicker shells, we observe a rapid deepening of the OC which preserves axisymmetry—we refer to this as secondary invagination (Fig. 2, $ii \rightarrow iii$). For higher $\bar{\theta}$, i.e., thinner shells, we observe that the second shape-shifting event consists of a loss of axisymmetry (Fig. 2, $II \rightarrow III$). We note that, for simulations that neglect mass changes, the symmetry-breaking event ($II \rightarrow III$) occurred for all $\bar{\theta}$, which means the normal morphogenesis process resulting in an axisymmetric OC cannot be modeled without mass addition. See SM [20] for OC formation movies.

To analyze, rationalize, and predict the qualitative features underlying the different shape-morphing pathways of OC morphogenesis, we used a shell model which accounts for growth as a stimulus that changes the rest length, i.e., natural stretch, and curvature, i.e., natural curvature of the shell's midsurface. The strain energy stored in the shell during growth is estimated based on updated rest midsurfaces. As a result, the natural curvature in the cap acts like a torque along the intersection between the cap and OOV to deform the OC [20]. When these natural quantities are homogeneous over some segment of shells, they can be represented by scalar values of Λ (stretch) and κ (curvature) whose specific values are calculated for each segment of the OC based on the experimentally measured growth characteristics (see SM for detailed derivation [20]), i.e., e_{ECM} and e_{IOV} for the bilayer cap, and e_{OOV} for the OOV. As a result, the cap and OOV have their own scalar values of natural stretch and curvature. The presence of Λ and κ imparts residual stresses in the growing OC, and these quantities play a similar role as external loads and torques do in classical mechanics, which can destabilize shells [55,56]. This suggests that OC morphogenesis may be governed by instabilities which result from residual stress that builds up during growth.

In the cap region, experimental observations note that the ECM and IOV grow at different rates. This through-thickness differential growth induces a natural curvature

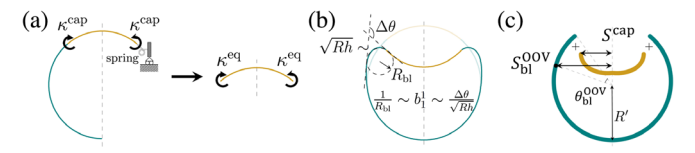


FIG. 3. (a) Equivalent natural curvature. (b) Geometrical characteristics on the OOV bending-dominated boundary layer. (c) Characteristic span of each separated cap and OOV.

that changes the apex of the OC from convex to concave. However, the inversion of this cap is resisted by the OOV which is a monolayer growing homogeneously and has to bend to accommodate the deforming cap. Open spherical shells experiencing an evolving natural curvature may exhibit a snap-through instability that everts the shell at a critical curvature [55]. Here, the OC is not an open shell, as the deformation of the cap will be resisted by the OOV. However, since the OOV is resisting bending, and therefore, resisting rotations imparted by the growth-induced torque along the intersection, we treated the OOV as an effective rotational spring [Fig. 3(a)]. Therefore, by way of a simple mechanical analogy, we model the full OC as an open spherical shallow shell, whose geometry is the same as the bilayer cap, experiencing an equivalent edge torque as shown in Fig. 3(a). The natural curvature in the cap due to differential growth, κ^{cap} , has to overcome the bending rigidity of the effective rotational spring [20], resulting in an equivalent natural curvature given by

$$\kappa^{\text{eq}} \sim \kappa^{\text{cap}} - \Gamma \frac{\Delta \theta}{\sqrt{Rh}},$$
(2)

where Γ is a dimensionless ratio of bending rigidities, i.e., $\Gamma = B^{\rm OOV}/[2B^{\rm cap}(1+\nu)]$ ($\Gamma = 0.06$ for the OC) with bending rigidities $B^{\rm cap}$ and $B^{\rm OOV}$ of the cap and OOV, respectively, and $\Delta\theta$ is angle change along the OOV boundary layer as shown in Fig. 3(b). Here, we assumed most of the OOV deformation occurs within its boundary layer as bending [57], and the second term on the rhs of (2) describes the amount that acts to bend the OOV boundary layer.

Open spherical shallow shells undergo snapping under homogeneous positive natural curvature when the boundary tangent vector in the colatitude direction becomes approximately horizontal, which results in $\kappa^{\rm eq}R \sim \bar{\theta}$ at the snapping [55]. Our numerical experiments here on closed spherical shells exhibit qualitatively similar behavior when the primary invagination occurs via snapping. That is, the primary invagination occurs when the colatitude-direction tangent vector at the intersection between the cap and OOV becomes approximately horizontal, which leads to $\Delta\theta \sim \alpha$ in (2) at the primary invagination. This results in a scaling law of the critical natural curvature in the cap at the primary invagination as

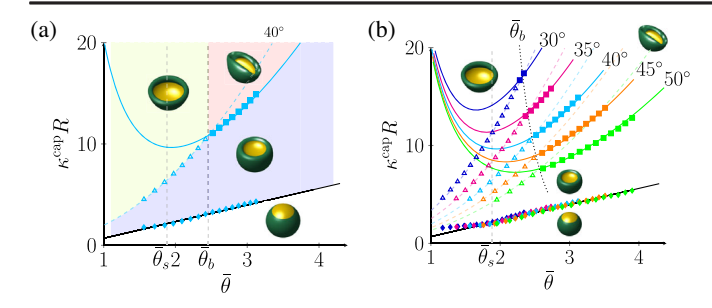


FIG. 4. (a) Phase diagram of instabilities during OC formation for varying R/h at $\alpha=40^\circ$. The blue region denotes the invaginated cup shape, and the lime and red regions are the normal (secondary invagination) and abnormal (buckling) OC, respectively. (b) Phase diagram for varying R/h and α . For (a) and (b), the symbols refer to simulation results, with diamonds symbolizing primary invagination, triangles for secondary invagination, and squares for buckling. The lines represent the scaling law of (3), (4), and (5). The black dotted line in (b) shows the buckling transition point $\bar{\theta}_b$ of (6).

$$\kappa_1^{\text{cap}} R = a_1 (1 + \Gamma) \bar{\theta} + b_1, \tag{3}$$

where a_1 and b_1 are scaling coefficients determined by our numerical simulations, which confirms the linear scaling with $\bar{\theta}$, and identifies the scaling coefficients as $a_1 = 1.55$ and $b_1 = -0.95$ [black solid line in Fig. 4(a)]. As with open shells, the primary invagination via snapping will only occur if $\bar{\theta} > \bar{\theta}_s (= [10/(1-\nu^2)]^{1/4})$ where $\bar{\theta}_s = 1.88$ for the OC [20], in good agreement with prior work [55] as the bending-dominated boundary layer covers the entire shell for $\bar{\theta} < \bar{\theta}_s$.

Following this primary invagination, growth and development of the OC continue until a second shape-shifting event occurs, which appears to be strongly correlated to the OC geometry. Thicker shells undergo a secondary invagination, forming a deep cup that facilitates normal eye development, while slender shells lose axisymmetry, forming a shape that may hinder normal OC morphogenesis. First, we consider the onset of secondary invagination. The magnitude of the torque at the intersection between the cap and OOV continues to increase due to the continued differential growth of the ECM and IOV. The OOV is not rigid, and therefore, the torque can either bend the OOV or further bend the cap. Building on the concept of a geometric composite [58], we can consider the growing cap and OOV as separate structures and, then, determine how they will deform when combined together. The cap, when removed from the OC, would form a shallow shell that spans a characteristic distance S^{cap} [Fig. 3(c)—yellow]. The OOV, when removed from the OC, would form a deep spherical shell of radius $R' = e_{OOV}R$, which is current radius as a result of growth. From our numerical simulations, we note that the extent of the OOV boundary layer, where bending deformations are concentrated, is constant until the secondary invagination occurs. We can estimate the characteristic span $S_{\rm bl}^{\rm OOV}$ of the OOV from the extent of its boundary layer [Fig. 3(c)—blue], and observe that, during secondary invagination, the OOV boundary layer increases in length and curvature. Therefore, we posit that when the span of the cap exceeds the span of the OOV boundary layer, the OC will undergo secondary invagination to account for this excess length.

The characteristic span of this OOV segment scales as $S_{\rm bl}^{\rm OOV} \sim R' \sin(\alpha + \theta_{\rm bl}^{\rm OOV})$ where $\theta_{\rm bl}^{\rm OOV}$ is angle subtended by the OOV boundary layer, which scales as $\theta_{\rm bl}^{\rm OOV} \sim \sqrt{h/R}$ for spherical shells [54]. The span of the cap scales as $S^{\rm cap} \sim R\alpha[1+\chi(1+\nu)h\kappa^{\rm cap}]$, where $\chi=[1+m(3n-2)]/(6mn)$ [20]. If we suppose that the critical point occurs when the spans are equivalent, i.e., $S_{\rm bl}^{\rm OOV} = S^{\rm cap}$, we obtain that the critical natural curvature is proportional to the shell geometry as $\kappa^{\rm cap}R \propto R/h$ from which the critical natural curvature in the cap at secondary invagination can be estimated as

$$\kappa_2^{\text{cap}} R \propto \frac{R}{h} = a_2 \frac{\bar{\theta}^2}{\sigma^2} + b_2,$$
(4)

where a_2 and b_2 are obtained from simulations to be $a_2 = 0.86$ and $b_2 = 0.22$. These parameters capture well the secondary invagination via the dashed color line in Fig. 4(a). Notably, unlike the primary invagination given by (3), the secondary invagination depends on opening angle α .

While our model predicts the morphogenetic process of OC formation via the experimentally observed [9,10] twostep (primary and secondary) invagination, it also indicates that very slender initial OC geometries will undergo an elastic instability that breaks axisymmetry, leading to abnormal OC development. This loss of the OC axisymmetry has been observed for glaucoma in newborn infants [19]. Secondary invagination occurs when the OOV boundary layer is flexible enough to bend to accommodate the excess length of the growing cap. If the OOV is too stiff, the cap must bend, instead. If we presume that the loss of axisymmetry for slender optic cups is due to a buckling instability, then the critical natural curvature can be analytically calculated via a linear stability analysis, which, for a circular plate with natural curvature κ^p and radius R^p , gives $\kappa^p h = \pm a_b (h/R^p)^2$ with $a_b = \chi(5 + 3\nu)/(1 - \nu^2)$ at the buckling instability $(a_b = 4.17 \text{ for the OC})$ [20]. To connect this critical natural curvature to open spherical shallow shells, we substitute $R^p \to R\alpha$. This gives us $\kappa^{\text{eq}}R \sim a_h/\bar{\theta}^2 + 1$, which is similar to [55]. Furthermore, the spherical shell's geometry under a torque induced by natural curvature leads to $\Delta\theta \sim \sqrt{R/h}$ in (2) at the buckling instability [20]. Then, the critical natural curvature in the cap at the buckling instability is given by

$$\kappa_b^{\rm cap} R = b_b \left(\frac{a_b}{\bar{\theta}^2} + 1 + \Gamma \alpha_2 \frac{\bar{\theta}^2}{\alpha^2} \right) + c_b, \tag{5}$$

where $\alpha_2(=\pi-\alpha)$ is a prefactor to treat the deep OOV shell, and b_b and c_b are scaling coefficients which provide the best fit with our simulations through $b_b=4.72$ and $c_b=-5.50$ via the solid color line in Fig. 4(a).

As our numerical experiments indicate that both secondary invagination and symmetry-breaking buckling cannot occur for the same initial geometry, the intersection between (4) and (5) gives us the transition point from secondary invagination to buckling as

$$\bar{\theta}_b = \sqrt{\frac{\sqrt{4\alpha^2 b_b a_b (a_2 - \alpha_2 b_b \Gamma) + \alpha^4 (c_b - b_2 + b_b)^2 + \alpha^2 (c_b - b_2 + b_b)}{2(a_2 - \alpha_2 b_b \Gamma)}},$$
(6)

where $\bar{\theta}_b=2.46$ is calculated at $\alpha=40^\circ$, in agreement with the numerical results $(\bar{\theta}_b=2.51)$.

Similar to the various R/h in biological situations, it is natural to think that the opening angle will also vary with diverse biological cues. The simulation results with various opening angles for a wide range from 30° to 50° are plotted on a phase diagram in Fig. 4(b) which fully characterizes the instability-induced shape morphing of the OC during its morphogenesis for a variety of initial geometries, showing that the proposed scaling laws work well for all α . Above the value of $\bar{\theta}_b$, denoted as the dashed black line via (6), the final OC shape is abnormal for each α .

In summary, we revealed the significant role that elastic instabilities play during OC morphogenesis. Because our model is predictive based on the initial geometry, we hope that our study will motivate experimental efforts to measure radius R, thickness h, and opening angle α of the initial OV to investigate their effects on OC morphogenesis and to verify the accuracy of our model predictions.

J.-H. L., H. S. P., and D. P. H. gratefully acknowledge financial support from the National Science Foundation through Grant No. CMMI-1824882.

- *parkhs@bu.edu †dpholmes@bu.edu
- [1] E. J. Pearl, J. Li, and J. B. Green, Cellular systems for epithelial invagination, Phil. Trans. R. Soc. B **372**, 20150526 (2017).
- [2] S. E. Skalicky, A. J. White, J. R. Grigg, F. Martin, J. Smith, M. Jones, C. Donaldson, J. E. Smith, M. Flaherty, and R. V. Jamieson, Microphthalmia, anophthalmia, and coloboma and associated ocular and systemic features: Understanding the spectrum, JAMA Ophthalmol. 131, 1517 (2013).
- [3] H. Lee, R. Khan, and M. OKeefe, Aniridia: Current pathology and management, Acta Ophthalmol. 86, 708 (2008).
- [4] C.-J. Zhou, A. Molotkov, L. Song, Y. Li, D. E. Pleasure, S. J. Pleasure, and Y.-Z. Wang, Ocular coloboma and dorsoventral neuroretinal patterning defects in Lrp6 mutant eyes, Dev. Dyn. 237, 3681 (2008).

- [5] S. Fuhrmann, Eye morphogenesis and patterning of the optic vesicle, in *Current Topics in Developmental Biology* (Elsevier, New York, 2010), Vol. 93, pp. 61–84.
- [6] D. Rosen and N. Mahabadi, Embryology, optic cup, in StatPearls [Internet] (StatPearls Publishing, Florida, 2019).
- [7] R. Hendrix and J. Zwaan, Changes in the glycoprotein concentration of the extracellular matrix between lens and optic vesicle associated with early lens differentiation, Differentiation (Berlin) 2, 357 (1974).
- [8] C. D. Bryan, M. A. Casey, R. L. Pfeiffer, B. W. Jones, and K. M. Kwan, Optic cup morphogenesis requires neural crest-mediated basement membrane assembly, Development 147, dev181420 (2020).
- [9] A. Oltean, J. Huang, D. C. Beebe, and L. A. Taber, Tissue growth constrained by extracellular matrix drives invagination during optic cup morphogenesis, Biomech. Model. Mechanobiol. 15, 1405 (2016).
- [10] H. S. Hosseini and L. A. Taber, How mechanical forces shape the developing eye, Prog. Biophys. Molec. Biol. 137, 25 (2018).
- [11] R. Adler and M. V. Canto-Soler, Molecular mechanisms of optic vesicle development: Complexities, ambiguities and controversies, Dev. Biol.305, 1 (2007).
- [12] J. Hyer, J. Kuhlman, E. Afif, and T. Mikawa, Optic cup morphogenesis requires pre-lens ectoderm but not lens differentiation, Dev. Biol. **259**, 351 (2003).
- [13] M. Eiraku, N. Takata, H. Ishibashi, M. Kawada, E. Sakakura, S. Okuda, K. Sekiguchi, T. Adachi, and Y. Sasai, Selforganizing optic-cup morphogenesis in three-dimensional culture, Nature (London) 472, 51 (2011).
- [14] T. Nakano, S. Ando, N. Takata, M. Kawada, K. Muguruma, K. Sekiguchi, K. Saito, S. Yonemura, M. Eiraku, and Y. Sasai, Self-formation of optic cups and storable stratified neural retina from human ESCs, Cell Stem Cell 10, 771 (2012).
- [15] K. M. Kwan, H. Otsuna, H. Kidokoro, K. R. Carney, Y. Saijoh, and C.-B. Chien, A complex choreography of cell movements shapes the vertebrate eye, Development 139, 359 (2012).
- [16] W. A. Harris and V. Hartenstein, Neuronal determination without cell division in Xenopus embryos, Neuron **6**, 499 (1991).
- [17] J. R. Martinez-Morales and J. Wittbrodt, Shaping the vertebrate eye, Curr. Opin. Genet. Dev. 19, 511 (2009).
- [18] S. Okuda, N. Takata, Y. Hasegawa, M. Kawada, Y. Inoue, T. Adachi, Y. Sasai, and M. Eiraku, Strain-triggered

- mechanical feedback in self-organizing optic-cup morphogenesis, Sci. Adv. 4. eaau1354 (2018).
- [19] K. T. Richardson, Optic cup symmetry in normal newborn infants, Invest. Ophthalmol. Visual Sci. 7, 137 (1968), https:// iovs.arvojournals.org/article.aspx?articleid=2128431.
- [20] See Supplemental Material at http://link.aps.org/supplemental/10.1103/PhysRevLett.127.138102 for a detailed derivation, which includes Refs. [21–28].
- [21] R. A. Sauer and T. X. Duong, On the theoretical foundations of thin solid and liquid shells, Math. Mech. Solids 22, 343 (2017).
- [22] F. Roohbakhshan and R. A. Sauer, Efficient isogeometric thin shell formulations for soft biological materials, Biomech. Model. Mechanobiol. 16, 1569 (2017).
- [23] E. Efrati, E. Sharon, and R. Kupferman, Elastic theory of unconstrained non-Euclidean plates, J. Mech. Phys. Solids 57, 762 (2009).
- [24] W. T. Koiter and J. G. Simmonds, Foundations of shell theory, in *Theoretical and Applied Mechanics* (Springer, New York, 1973), pp. 150–176.
- [25] M. Pezzulla, N. Stoop, X. Jiang, and D.P. Holmes, Curvature-driven morphing of non-Euclidean shells, Proc. R. Soc. A 473, 20170087 (2017).
- [26] A. Lucantonio, P. Nardinocchi, and M. Pezzulla, Swelling-induced and controlled curving in layered gel beams, Proc. R. Soc. A 470, 20140467 (2014).
- [27] M. Pezzulla, G. P. Smith, P. Nardinocchi, and D. P. Holmes, Geometry and mechanics of thin growing bilayers, Soft Matter 12, 4435 (2016).
- [28] W. T. Koiter and A. Van Der Heijden, WT Koiter's Elastic Stability of Solids and Structures (Cambridge University Press, Cambridge; New York, NY, USA 2009).
- [29] S. Höhn, A. R. Honerkamp-Smith, P. A. Haas, P. K. Trong, and R. E. Goldstein, Dynamics of a Volvox Embryo Turning Itself Inside Out, Phys. Rev. Lett. 114, 178101 (2015).
- [30] P. A. Haas, S. M. H. Hohn, A. R. Honerkamp-Smith, J. B. Kirkegaard, and R. E. Goldstein, The noisy basis of morphogenesis: Mechanisms and mechanics of cell sheet folding inferred from development variability, PLOS Biol. 16, e2005536 (2018).
- [31] P. A. Haas and R. E. Goldstein, Morphoelasticity of large bending deformations of cell sheets during development, Phys. Rev. E **103**, 022411 (2021).
- [32] G. Chagnon, M. Rebouah, and D. Favier, Hyperelastic energy densities for soft biological tissues: A review, J. Elast. **120**, 129 (2015).
- [33] S. Budday, G. Sommer, C. Birkl, C. Langkammer, J. Haybaeck, J. Kohnert, M. Bauer, F. Paulsen, P. Steinmann, E. Kuhl *et al.*, Mechanical characterization of human brain tissue, Acta Biomater. **48**, 319 (2017).
- [34] E. K. Rodriguez, A. Hoger, and A. D. McCulloch, Stress-dependent finite growth in soft elastic tissues, J. Biomech. 27, 455 (1994).
- [35] A. Goriely, The Mathematics and Mechanics of Biological Growth (Springer, New York, 2017), Vol. 45.
- [36] E. Kuhl, Growing matter: A review of growth in living systems, J. Mech. Behav. Biomed. Mater. 29, 529 (2014).

- [37] V. A. Lubarda and A. Hoger, On the mechanics of solids with a growing mass, Int. J. Solid Struct. 39, 4627 (2002).
- [38] T. X. Duong, F. Roohbakhshan, and R. A. Sauer, A new rotation-free isogeometric thin shell formulation and a corresponding continuity constraint for patch boundaries, Comput. Methods Appl. Mech. Eng. **316**, 43 (2017).
- [39] A. V. De Reuck and J. Knight, *Colour Vision: Physiology* and *Experimental Psychology* (John Wiley & Sons, New York, 2009), Vol. 965.
- [40] S. R. Hilfer, R. C. Brady, and J.-J. W. Yang, Intracellular and extracellular changes during early ocular development in the chick embryo, in *Ocular Size and Shape Regulation During Development* (Springer, New York, 1981), pp. 47–78.
- [41] H. S. Hosseini, D. C. Beebe, and L. A. Taber, Mechanical effects of the surface ectoderm on optic vesicle morphogenesis in the chick embryo, J. Biomech. 47, 3837 (2014).
- [42] A. Djellouli, P. Marmottant, H. Djeridi, C. Quilliet, and G. Coupier, Buckling Instability Causes Inertial Thrust for Spherical Swimmers at All Scales, Phys. Rev. Lett. 119, 224501 (2017).
- [43] A. G. Holzapfel, *Nonlinear Solid Mechanics II* (John Wiley & Sons, New York, 2000).
- [44] M. Ben Amar and A. Goriely, Growth and instability in elastic tissues, J. Mech. Phys. Solids **53**, 2284 (2005).
- [45] G. Xu, P. S. Kemp, J. A. Hwu, A. M. Beagley, P. V. Bayly, and L. A. Taber, Opening angles and material properties of the early embryonic chick brain, J. Biomech. Eng. 132, 011005 (2010).
- [46] E. Uchio, S. Ohno, J. Kudoh, K. Aoki, and L. T. Kisiele-wicz, Simulation model of an eyeball based on finite element analysis on a supercomputer, British Journal of Ophthalmology 83, 1106 (1999).
- [47] I. A. Sigal, J. G. Flanagan, and C. R. Ethier, Factors influencing optic nerve head biomechanics, Invest. Ophthalmol. Visual Sci. **46**, 4189 (2005).
- [48] E. A. Bassett, T. Williams, A. L. Zacharias, P. J. Gage, S. Fuhrmann, and J. A. West-Mays, Ap- 2α knockout mice exhibit optic cup patterning defects and failure of optic stalk morphogenesis, Human Molecular Genetics **19**, 1791 (2010).
- [49] L.-Y. Wu, M. Li, D. R. Hinton, L. Guo, S. Jiang, J. T. Wang, A. Zeng, J. B. Xie, M. Snead, C. Shuler *et al.*, Microphthalmia resulting from *M sx2*-induced apoptosis in the optic vesicle, Invest. Ophthalmol. Visual Sci. **44**, 2404 (2003).
- [50] Y. Ishii, K. Weinberg, I. Oda-Ishii, L. Coughlin, and T. Mikawa, Morphogenesis and cytodifferentiation of the avian retinal pigmented epithelium require down-regulation of Group B1 Sox genes, Development 136, 2579 (2009).
- [51] F. Müller, H. Rohrer, and A. Vogel-Höpker, Bone morphogenetic proteins specify the retinal pigment epithelium in the chick embryo, Development **134**, 3483 (2007).
- [52] T. Pandit, V. K. Jidigam, C. Patthey, and L. Gunhaga, Neural retina identity is specified by lens-derived BMP signals, Development **142**, 1850 (2015).

- [53] Y. Hasegawa, N. Takata, S. Okuda, M. Kawada, M. Eiraku, and Y. Sasai, Emergence of dorsal-ventral polarity in esc-derived retinal tissue, Development **143**, 3895 (2016).
- [54] F. I. Niordson, Shell Theory (Elsevier, New York, 2012).
- [55] M. Pezzulla, N. Stoop, M. P. Steranka, A. J. Bade, and D. P. Holmes, Curvature-Induced Instabilities of Shells, Phys. Rev. Lett. 120, 048002 (2018).
- [56] D. P. Holmes, J.-H. Lee, H. S. Park, and M. Pezzulla, Nonlinear buckling behavior of a complete spherical shell
- under uniform external pressure and homogenous natural curvature, Phys. Rev. E **102**, 023003 (2020).
- [57] E. Efrati, E. Sharon, and R. Kupferman, Buckling transition and boundary layer in non-Euclidean plates, Phys. Rev. E **80**, 016602 (2009).
- [58] M. Pezzulla, S. A. Shillig, P. Nardinocchi, and D. P. Holmes, Morphing of geometric composites via residual swelling, Soft Matter 11, 5812 (2015).

SUPPORTING INFORMATION: Elastic Instabilities Govern the Morphogenesis of the Optic Cup

Jeong-Ho Lee, ¹ Harold S. Park, ¹, * and Douglas P. Holmes¹, [†]

¹Department of Mechanical Engineering, Boston University, Boston, MA, 02215.

I. SHELL KINEMATICS

The mechanical system for the optic cup (OC) formation is modeled as a nonlinear Kirchhoff–Love shell. When a curved surface (shell) with thickness h is considered in three–dimensional space, its material points are described by a general mapping from a parametric domain on the mid-surface [1]. The general mapping of the current shell configuration Ω from the parametric domain is expressed by $\mathbf{r} = \mathbf{x} \mid_{\xi^3 = 0} = \mathbf{r}(\xi^{\alpha})$ using the curvilinear coordinates ξ^i embedded in the thin surface where \mathbf{r} and \mathbf{x} are the position vectors on the mid-surface and the 3D surface body, respectively. In this letter, Latin indices take 1,2,3, and Greek indices are restricted to 1,2. Based on the parameterization, the covariant tangent vectors are obtained on the mid-surface by (S1) using the parametric derivative.

$$a_{\alpha} = r_{,\alpha} = \frac{\partial r}{\partial \xi^{\alpha}}$$
 (S1)

Then, the surface normal vector is calculated using the covariant tangent vectors by (S2), which is called the *director* in the Kirchhoff-Love shell theory.

$$n = a_3 = a^3 = \frac{a_1 \times a_2}{\parallel a_1 \times a_2 \parallel}$$
 (S2)

Using the obtained tangent vectors, the 2D metric tensor (first fundamental form) with covariant and contravariant components are calculated by (S3) and (S4). These contain information about lateral distances between material points on the mid-surface.

$$a_{\alpha\beta} = \boldsymbol{a}_{\alpha} \cdot \boldsymbol{a}_{\beta}$$
 (S3)

$$[a^{\alpha\beta}] = [a_{\alpha\beta}]^{-1} \tag{S4}$$

To express information about the local curvature of the mid-surface, the curvature tensor (second fundamental form) is calculated by (S5).

$$b_{\alpha\beta} = \mathbf{n} \cdot \mathbf{a}_{\alpha\beta} = -\mathbf{n}_{\beta} \cdot \mathbf{a}_{\alpha} \tag{S5}$$

In the same manner, the mid-surface definitions on the initial shell configuration Ω_0 can be calculated using the initial position vector \mathbf{r}_0 instead of \mathbf{r} , such as $\mathring{a}_{\alpha\beta}$ and $\mathring{b}_{\alpha\beta}$, with the overcircle denoting quantities associated with the initial body.

To deal with multi-layer shell problems, the 3D stored strain energy is, in this letter, projected onto the mid-surface [2], in accordance with the stress constitutive equations derived from the first two thermodynamics laws. The physical meaning of this concept is to integrate the stress constitutive equation through the thickness direction with respect to each layer using the relation between the 3D metric tensor g_{ij} and the 2D fundamental forms of $a_{\alpha\beta}$ and $b_{\alpha\beta}$ with the chain rule. Based on one of the Kirchhoff-Love shell assumptions, i.e. that vectors which are initially normal to the mid-surface remain normal to the mid-surface after deformation, the current 3D position vector \boldsymbol{x} is analytically expressed as $\boldsymbol{x} = \boldsymbol{r} + \lambda_3 \xi^3 \boldsymbol{n}$ with the thickness-direction coordinate $\xi^3 : [-h/2, h/2]$ where λ_3 is a quantity which describes the thickness change during deformation. Then, the 3D metric tensor of the current surface has covariant components as $g_{ij} = (\partial \boldsymbol{x}/\partial \xi^i) \cdot (\partial \boldsymbol{x}/\partial \xi^j)$ leading to its in-plane components of $g_{\alpha\beta} = a_{\alpha\beta} - 2\lambda_3 \xi^3 b_{\alpha\beta} + O(h^2)$ with zero values for the out-of-plane shear deformation as

$$[g_{ij}] = \begin{bmatrix} (g_{\alpha\beta})_{2\times 2} & 0\\ 0 & (\lambda_3)^2 \end{bmatrix}. \tag{S6}$$

^{*} parkhs@bu.edu

[†] dpholmes@bu.edu

Using the relation between the 3D metric tensor and the 2D fundamental forms, the projected stress constitutive equations for the multi-layer surface are derived to calculate resultant stresses on the mid-surface, i.e. the membrane stress $\tau_{\sigma}^{\alpha\beta}$ and the bending stress $\tau_{M}^{\alpha\beta}$ as

$$\tau_{\sigma}^{\alpha\beta} = \sum_{l} \int_{h_{l}} \Sigma^{\gamma\delta} \frac{\partial g_{\gamma\delta}}{\partial a_{\alpha\beta}} d\xi^{3}$$
 (S7a)

$$\tau_M^{\alpha\beta} = \sum_{l} \int_{h_l} \Sigma^{\gamma\delta} \frac{\partial g_{\gamma\delta}}{\partial b_{\alpha\beta}} d\xi^3$$
 (S7b)

where the subscription l denotes the layer number, and \sum_l means that the resultant membrane and bending stresses on the mid-surface are the net stresses of the second Piola-Kirchhoff stress tensor Σ^{ij} for all layers projected on the mid-surface. Moreover, the thickness change-related quantity λ_3 can be analytically calculated based on the plane-stress condition, i.e. $\Sigma^{33}=0$, resulting from the Kirchhoff-Love shell assumptions, as shown in Fig. S1 which clearly shows that the change in thickness occurs differently in different parts of the OC (i.e. ECM, iOV, and oOV) due to differences in the mechanical properties and growth characteristics in each region. From the definition of the 3D metric tensor in the surface normal direction, the actual value of the thickness change in a layer during deformation can be obtained as $(\int_{h_b}^{h_t} \lambda_3 \ d\xi^3)/(h_t - h_b)$ where h_t and h_b are the top and bottom thickness coordinates of the layer, respectively.

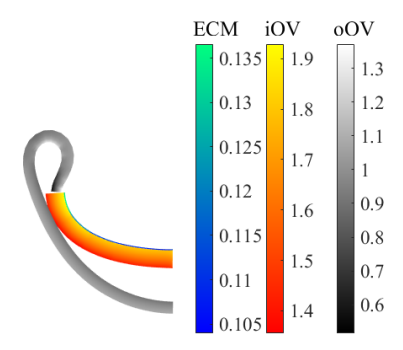


FIG. S1. The thickness change-related quantity λ_3 calculated through the plane-stress condition at the completion of the optic cup morphogenesis for initial radius-thickness ratio R/h = 5 and opening angle $\alpha = 40^{\circ}$, accounting for mass change.

In this letter, the hyperelastic neo-Hookean constitutive model is used for the stress constitution to consider the non-linear material behavior of compressible, soft elastic materials. The strain energy density is given by

$$\Psi_0 = \frac{\lambda}{4} (J_m^2 - 1 - 2\log J_m) + \frac{\mu}{2} (I_{m1} - 3 - 2\log J_m)$$
 (S8)

where $\lambda = \frac{E\nu}{(1+\nu)(1-2\nu)}$ and $\mu = \frac{E}{2(1+\nu)}$ are Lamé constants with Young's modulus E and Poisson's ratio ν , and I_{m1} and J_m are respectively the first and third (Jacobian) invariants of the right Cauchy-Green tensor $C_m = F_m^T F_m$ based on the multiplicative decomposition of the deformation gradient $F = F_m F_g$ in which F_m and F_g are respectively the mechanical and growth parts. The first term on RHS vanishes with $J_m = 1$, which gives the incompressible neo-Hookean form of $\Psi_0 = \frac{\mu}{2}(I_{m1} - 3)$ as the isochoric elastic response, whereas the second term goes to zero for $C_m = J_m^{2/3} I$ with the 3D identity tensor I as the volumetric elastic response. These shell kinematics and constitution are applied to solve the linear momentum balance equation to calculate the deformations of shells.

II. EXPANSION FACTOR DUE TO GROWTH e

Based on the multiplicative decomposition of the deformation gradient $F = F_m F_g$ in which F_m and F_g are respectively the mechanical and growth parts, F_g is utilized to construct the intermediate (stress-free) shell configuration $\tilde{\Omega}$ assuming isotropic area growth, as $F_g = eI + (1 - e)n_0 \otimes n_0$ with the expansion factor e owing to the mass change

during growth and the unit normal vector to the initial shell n_0 . In order to calculate the expansion factor e, which depends on the mass change during growth, the mass balance equation including mass source and flux is first solved for each layer as

$$\frac{d}{dt} \int_{\Omega} (h\rho) \ da = \int_{\Omega} (hS) \ da - \int_{\partial \Omega} (h\mathbf{f} \cdot \mathbf{m}) \ ds \tag{S9}$$

where ρ is the current mass density (i.e. the current mass divided by the current volume), S and f are the mass source and flux, respectively, m is the outward unit normal vector to the current boundary curve, and da and ds are the area and line element of the current shell, respectively.

Changes in the shell area, which are modeled using isotropic in-plane growth, occur due to mass increase or decrease that is associated with a specific amount of volume depending on the material density. As such, the expansion factor e associated with the isotropic area growth can be calculated by means of the volume of a unit mass v_m as

$$e = \sqrt{1 + v_m(J\rho - \rho_0)} \tag{S10}$$

where ρ_0 is the initial mass density (i.e. the initial mass divided by the initial volume), and J is the Jacobian for F. Note that density-preserving growth can be implemented as $v_m = 1/\rho_0$. Then, the intermediate (stress-free) 3D metric tensor is calculated as $\tilde{g}_{\alpha\beta} = \tilde{a}_{\alpha\beta} - 2\xi^3 \tilde{b}_{\alpha\beta}$ through $\tilde{a}_{\alpha\beta} = e^2 \mathring{a}_{\alpha\beta}$, $\tilde{b}_{\alpha\beta} = e^2 \mathring{b}_{\alpha\beta}$ for isotropic area growth, with the overtilde denoting quantities associated with the intermediate (stress-free) configuration of each layer in the 3D surface body, i.e.

$$[\tilde{g}_{ij}] = \begin{bmatrix} (\tilde{g}_{\alpha\beta})_{2\times2} & 0\\ 0 & 1 \end{bmatrix}. \tag{S11}$$

As described in the main text, the extracellular matrix (ECM), inner optic vesicle (iOV), and outer optic vesicle (oOV) all have different expansion factors depending on their biological growth rates that are prescribed based on experimental observations for each region [3].

III. STRESS AMPLIFICATION ACCORDING TO MASS CHANGE FROM GROWTH

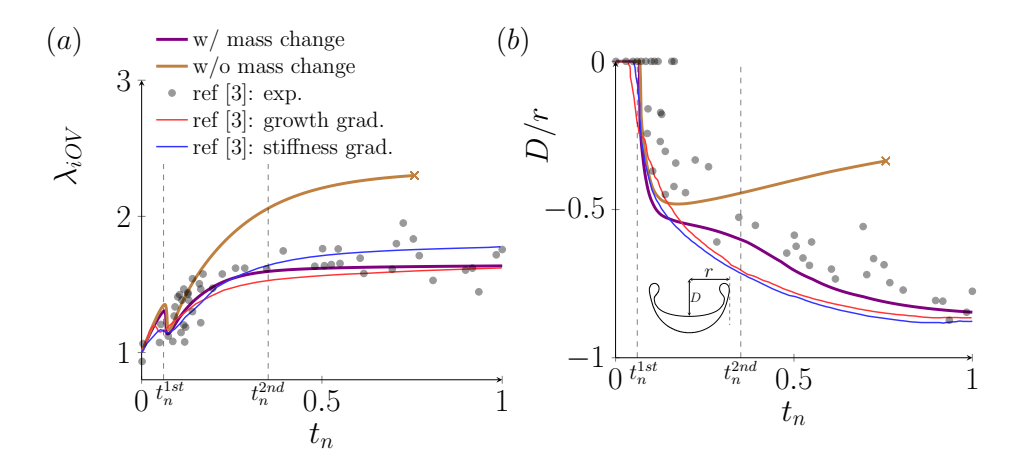


FIG. S2. Comparison of the OC formation characteristics for R/h = 5 and $\alpha = 40^{\circ}$ with and without the mass change effect, as in the current work, or assumed stiffness and material property gradients [3], for (a) center iOV thickness change ratio (λ_{iOV}) , and (b) normalized invagination depth (D/r).

Because mass is a variable that impacts the strain energy density over the initial configuration of the body, it is clear that any mass increase from growth should modify the internal stress of the body as the internal stress is calculated as the derivative of the strain energy density with respect to the strain. Because the internal stress is required to solve the balance of linear momentum, modifications of the stress due to added mass from growth may result in different deformation pathways as compared to when mass changes due to growth are neglected. In this section, we explain how mass changes due to growth alter the strain energy density and the stress, and apply this to the case

which corresponds to the case of OC formation (where the mass that is added during density-preserving growth is the same as the previously existing material). Here, we consider the effect of mass addition on the strain energy density and the stress for the biological growth case where the added mass has comparable mechanical properties, such as stiffness, to the existing material. From thermodynamics laws, the second Piola-Kirchhoff stress tensor Σ^{ij} is calculated as $\Sigma^{ij} = (J\rho)\partial\psi/\partial\epsilon_{ij}$ with the deformation-dependent free energy per mass ψ and the Green-Lagrange strain $\epsilon_{ij} = \frac{1}{2}(g_{ij} - \tilde{g}_{ij})$. When growth induces the change in mass of a body with the initial mass M_0 and volume V_0 , $J\rho$ is no longer the same as the initial density $\rho_0 = M_0/V_0$ but can be expressed as $J\rho = M/V_0 = (M_0 + \Delta M)/V_0$ where M and ΔM are the current mass and the amount of mass change from growth, respectively. This results in $\Sigma^{ij} = (\rho_0)\partial\psi/\partial\epsilon_{ij} + (\Delta M/V_0)\partial\psi^{\Delta M}/\partial\epsilon_{ij}$ in which the first term represents the standard second Piola-Kirchhoff stress, and the second term is an added term arising from the effect of the mass change from growth. Here, the superscript in $\psi^{\Delta M}$ indicates that this free energy corresponds to the material type associated with the newly added mass ΔM from growth. If the material type of the added mass from growth is the same as the existing initial material in the body, the mass change effect on the internal stress exists in the form of

$$\Sigma^{ij} = (J\rho) \frac{\partial \psi}{\partial \epsilon_{ij}} = \left(\frac{J\rho}{\rho_0}\right) \frac{\partial \Psi_0}{\partial \epsilon_{ij}} \tag{S12}$$

where $\Psi_0 = \rho_0 \psi$ is the free energy density that is standard in continuum mechanics [4]; we utilize the neo-Hookean free energy of (S8) in this work. Thus, the key result of (S12) is that mass change due to growth results in a stress amplification factor of $J\rho/\rho_0$ that modifies the state of stress in the body compared to standard continuum mechanics which does not account for mass change, assuming that the added material is the same as that of the original body. Note that density-preserving growth leads to $(J\rho)/\rho_0 = J_g = e^2$ where J_g is the growth Jacobian for \mathbf{F}_g , which coincides with Eq. (1) in the main text, as $J_m\rho = \rho_0$ from the definition of density-preserving growth where J_m is the mechanical Jacobian for \mathbf{F}_m . In this letter, we applied the amplified stress for the constitution to calculate the resultant mid-surface stresses of (S7).

Previous works modeling OC formation were done by prescribing either hypothetical stiffness or growth property gradients [3, 5]. In contrast, a key feature of the current approach is that the OC formation is obtained only considering stress amplification effects resulting from mass change during growth. We show in Fig. S2 that simply accounting for the mass change through the resulting stress amplification described in (S12) enables us to accurately capture experimental measurements of both the center iOV thickness change ratio (λ_{iOV}) and the normalized invagination depth (D/r) as a function of time without the hypothetical growth property gradients.

We note that previous works [6] have obtained a stress amplification similar to that shown in (S12), with the factor being $J = \det \mathbf{F}$. This extra factor is the same as the one in (S12) for a specific situation where 1) growth is density-preserving; 2) the added mass during growth is the same as the existing one; and 3) elastic deformation is incompressible. That is, the stress amplification factor e^2 in the optic cup case generalizes previous works [6]. However, because our study has considered the optic cup components to be compressible materials, based on experimental data, both the resulting physical interpretations and the mathematical origins of the stress amplification in (S12) are different than in reference [6].

Furthermore, since the approach in reference [6] computes the extra factor using elastic strains from the grown, and not reference state, it always gives the same stress amplification (= J) for all types of stimuli, such as heating, swelling, and growth, because it only depends upon the change in area or volume of the material under consideration. For a simple example of why this may cause issues, consider a material that is swelling by water. This material will be softer (i.e. its stiffness deceased). On the other hand, if this material is growing by mass addition using the same material as the existing one in the manner of density-preserving growth, this material's stiffness will be the same as before. However, using the amplification of Ben Amar and Goriely would lead to the same stress amplification for these very different physical situations. In contrast, the stress amplification we derived that is represented by the density ratio $(J\rho/\rho_0)$ which goes to e^2 in the case of the optic cup growth) can describe the stiffness difference between the stimulus types in terms of the mass addition as $J\rho = \rho_0$ for the cases where there is no mass addition with comparable mechanical properties. For example, as heating does not induce a change in mass, there is no stress amplification, which is consistent with the mass balance equation when $J\rho = \rho_0$ such that the stress amplification factor $J\rho/\rho_0=1$. For swelling, because the stiffness of the absorbed fluid is negligible, this leads to the mass balance equation $J\rho = \rho_0$ such that the stress amplification factor $J\rho/\rho_0=1$.

IV. SHELL ENERGY WITH EXTERNAL LOADS INDUCED BY GROWTH

Biological growth gives rise to residual stresses in the body, and these stresses dictate deformations [7]. This fact implies that growth plays a role equivalent to external loading. In this section, the contribution of growth is described as external loads with reference to natural stretching Λ and curvature κ , which contain information related to the

rest length and curvature of the mid-surface, and applied to the problem of OC formation. This helps to understand how differential growth during OC formation works in terms of mechanical deformations.

The shell energy W stored by deformations induced by growth can be calculated by employing Non-Euclidean shell theory [8]. Here, the membrane strain is $\bar{E}_{\alpha\beta} = \frac{1}{2}(a_{\alpha\beta} - \bar{a}_{\alpha\beta})$ and the bending strain is $\bar{K}_{\alpha\beta} = b_{\alpha\beta} - \bar{b}_{\alpha\beta}$ in which an updated rest mid-surface defined with $\bar{a}_{\alpha\beta}$ and $\bar{b}_{\alpha\beta}$ is used to represent an equivalent stress-free shell configuration $\bar{\Omega}$ depending on the growth profile of the body. This results in a shell energy of

$$W = \int \frac{Y}{2} (\nu \bar{a}^{\alpha\lambda} \bar{a}^{\beta\mu} \bar{E}_{\lambda\alpha} \bar{E}_{\mu\beta} + (1 - \nu) \bar{a}^{\alpha\lambda} \bar{a}^{\beta\mu} \bar{E}_{\lambda\beta} \bar{E}_{\mu\alpha}) + \frac{B}{2} (\nu \bar{a}^{\alpha\lambda} \bar{a}^{\beta\mu} \bar{K}_{\lambda\alpha} \bar{K}_{\mu\beta} + (1 - \nu) \bar{a}^{\alpha\lambda} \bar{a}^{\beta\mu} \bar{K}_{\lambda\beta} \bar{K}_{\mu\alpha}) d\bar{a}$$
 (S13)

where $Y=\frac{Eh}{1-\nu^2}$ and $B=\frac{Eh^3}{12(1-\nu^2)}$ are respectively the membrane and bending rigidities, and $d\bar{a}$ is the area element of the updated rest shell. For homogeneous natural stretching and curvature over some shell segment, the natural fundamental forms can be written as $\bar{a}_{\alpha\beta}=\Lambda^2\mathring{a}_{\alpha\beta}$ and $\bar{b}_{\alpha\beta}=\Lambda^2\mathring{b}_{\alpha\beta}+\Lambda^2\kappa\mathring{a}_{\alpha\beta}$. The specific values of Λ and κ depend on the segment's growth characteristics. After some algebra utilizing the linear terms of the membrane and bending strains with respect to displacement, this shell energy can be rewritten in order to embody external loads induced by growth, which for spherical shells is

$$W = \Lambda^{-2}W_K - P_V^{bulk} - P_V^{edge} - P_B^{bulk} - P_B^{edge}$$
(S14a)

$$P_Y^{bulk} = \int Y(1+\nu) \frac{1}{R} (1-\Lambda^{-2}) w \, da_0$$
 (S14b)

$$P_Y^{edge} = \oint Y(1+\nu)\frac{1}{2} \left(1 - \Lambda^{-2}\right) \boldsymbol{u} \cdot \boldsymbol{m}_0 \, ds_0 \tag{S14c}$$

$$P_B^{bulk} = \int 2B(1+\nu) \left(1 - \Lambda^{-2} - \kappa R\right) \frac{w}{R^3} da_0$$
 (S14d)

$$P_B^{edge} = \oint B(1+\nu) \frac{1}{R} \left(1 - \Lambda^{-2} - \kappa R \right) \left(\frac{\boldsymbol{u}}{R} - \boldsymbol{q} \right) \cdot \boldsymbol{m}_0 \, ds_0$$
 (S14e)

where W_K is the standard Koiter shell potential energy based on deformations between the current and initial shell configurations [9], w and w are respectively the normal and in-plane displacements, m_0 is the outward unit normal vector to the initial boundary curve, q is the rotation vector representing the rotation of an element of the shell, and da_0 and ds_0 are the area and length element of the initial shell, respectively. Note that the prefactor Λ^{-2} in front of W_K comes from considering the undeformed, reference configuration as a stress-free configuration to be consistent with conventional continuum mechanics. From these non-mechanical load terms in (S14b-S14e), one can confirm that the natural stretching and curvature act like pressure, traction and boundary torques, i.e. external loads due to growth, to morph the body. For spherical shells with $h/R \ll 1$, $Y \propto h$ and $B \propto h^3$ yield that the contribution of P_B^{edge} in terms of $q \cdot m_0$ is dominant among the external terms, i.e.

$$W = \Lambda^{-2}W_K - \oint B(1+\nu)\frac{1}{R} \left[\kappa R - (1-\Lambda^{-2})\right] \boldsymbol{q} \cdot \boldsymbol{m}_0 \ ds_0$$
 (S15)

which indicates that the natural stretching and curvature act like a torque along the open edge of the shell as $\mathbf{q} \cdot \mathbf{m}_0$ gives a change in the tangent angle of the shell [10].

V. Λ AND κ ON THE OPTIC CUP

Based on the differential growth rate of the OC, its geometry can be divided into two parts: the cap region (iOV+ECM) and the oOV, and each part has its own homogeneous natural quantities Λ and κ according to their experimentally measured growth characteristics. In this section, we derive analytical equations to calculate Λ and κ for specific growth characteristics of bi-layer surfaces with consideration for the mass changes during growth. We then apply the derived equations for the cap region and the oOV to obtain their natural quantity set, i.e. $\{\Lambda^{cap}, \kappa^{cap}\}$ for the cap and $\{\Lambda^{oOV}, \kappa^{oOV}\}$ for the oOV, in which the potential energy stored during OC morphogenesis can be

calculated as $W^{OC} = W^{cap} + W^{oOV}$ where W^{cap} and W^{oOV} are the energies of the cap and oOV that are obtained by inserting their natural quantity set into (S15). A few equations for the natural quantities have been proposed, for example, [11] via the linear geometrical projection and [12] via 1D beam theory. However, both [11] and [12] did not consider the multidimensional features of shells as well as the mass change effect from biological growth.

As previously discussed, the isotropic area growth of a surface layer with expansion factor e locally has the stress-free shell configuration represented by the 3D metric tensor $\tilde{g}_{\alpha\beta}=e^2(\mathring{a}_{\alpha\beta}-2\xi^3\mathring{b}_{\alpha\beta})$ for its in-plane components. Then, when an infinitesimal bi-layer shell element with thickness h is growing with e_1 and e_2 on the upper and lower layers, respectively, the Koiter-like strain energy density Ψ_{proj} between the deformed and stress-free body can be calculated using the in-plane components of the Green-Lagrange strain $\epsilon_{\alpha\beta}=\frac{1}{2}(g_{\alpha\beta}-\tilde{g}_{\alpha\beta})$ via the thickness-direction integration with the plane-stress condition as

$$\Psi_{proj} = \int_{h/2 - h_1}^{h/2} \frac{1}{2} \left(\rho^r A^{\alpha\beta\gamma\delta} \epsilon_{\alpha\beta} \epsilon_{\gamma\delta} \right)_1 d\xi^3 + \int_{-h/2}^{-h/2 + h_2} \frac{1}{2} \left(\rho^r A^{\alpha\beta\gamma\delta} \epsilon_{\alpha\beta} \epsilon_{\gamma\delta} \right)_2 d\xi^3$$
 (S16)

where the subscript numbers 1 and 2 denote the upper and lower layer, respectively, and $\rho^r = J\rho/\rho_0$ is the density ratio which is the stress amplification factor due to the mass change as stated above, and $A^{\alpha\beta\gamma\delta} = \lambda \tilde{g}^{\alpha\beta} \tilde{g}^{\gamma\delta} + \mu (\tilde{g}^{\alpha\gamma} \tilde{g}^{\beta\delta} + \tilde{g}^{\alpha\delta} \tilde{g}^{\beta\gamma})$ is the elasticity tensor with $\tilde{g}^{\alpha\beta} = [\tilde{g}_{\alpha\beta}]^{-1}$.

Based on the definition of the rest mid-surface, the shell becomes a stress-free state for both (S13) and (S16) such that for mid-surface stresses, $2\partial\Psi_{proj}/\partial a_{\alpha\beta}=0$ of the membrane stress and $\partial\Psi_{proj}/\partial b_{\alpha\beta}=0$ of the bending stress at $a_{\alpha\beta}=\bar{a}_{\alpha\beta}$ and $b_{\alpha\beta}=\bar{b}_{\alpha\beta}$ with an assumption of small thickness change. Then, the natural quantities Λ and κ can be derived with respect to the thickness ratio $m=h_1/h_2$ and the moduli ratio $n=\mu_1/\mu_2=E_1/E_2$ for thin spherical shells, i.e. $h/R\ll 1$ as

$$\Lambda^{2} = \frac{e_{1}^{2}e_{2}^{8}m^{4}n^{2}\rho_{1}^{r^{2}} + e_{1}^{4}e_{2}^{4}mn\left(e_{1}^{2}(3m(m+1)+1) + e_{2}^{2}(m(m+3)+3)\right)\rho_{1}^{r}\rho_{2}^{r} + e_{1}^{8}e_{2}^{2}\rho_{2}^{r^{2}}}{e_{2}^{8}m^{4}n^{2}\rho_{1}^{r^{2}} + 2e_{1}^{4}e_{2}^{4}m(m(2m+3)+2)n\rho_{1}^{r}\rho_{2}^{r} + e_{1}^{8}\rho_{2}^{r^{2}}}$$
(S17)

$$\kappa = -\frac{1}{h} \frac{3e_1^4 e_2^4 \left(e_1^2 - e_2^2\right) m(m+1)^2 n \rho_1^r \rho_2^r}{\left(e_2^8 m^4 n^2 \rho_1^{r^2} + 2e_1^4 e_2^4 m(m(2m+3) + 2) n \rho_1^r \rho_2^r + e_1^8 \rho_2^{r^2}\right) \Lambda^2}.$$
 (S18)

In the case of the density-preserving and isotropic area growth we are considering in this letter, the density ratio ρ^r corresponds to $\rho_1^r = e_1^2$ and $\rho_2^r = e_2^2$ for each layer as aforementioned above, whereas $\rho_1^r = \rho_2^r = 1$ means to ignore the mass change. Note that since these calculations have been locally done on the infinitesimal shell element, this derivation process shall be carried out without consideration for the surface compatibility constraints like the Gauss-Codazzi-Mainardi equations.

Therefore, inserting specific values of $e_1 \to e_{ECM}$ and $e_2 \to e_{iOV}$ gives the natural quantities (Λ^{cap} and κ^{cap}) for the cap region with consideration for the mass change effect. Additionally, these analytical equations can be also applied for mono-layer surfaces by using $m \to 0$ to calculate their natural stretching and curvature. Then, inserting $e_2 \to e_{oOV}$ with $m \to 0$ yields that $\Lambda^{oOV} = e_{oOV}$ and $\kappa^{oOV} = 0$ for the mono-layer oOV.

From these calculated natural quantities on the OC, one can get $1 - \Lambda^{cap^{-2}} \ll \kappa^{cap} R$ and $1 - \Lambda^{oOV^{-2}} \ll \kappa^{cap} R$ due to the OC growth characteristics, i.e. $e_{ECM} = 1$, $e_{iOV} = 1 + 5t_n$, and $e_{oOV} = 1 + 1.5t_n$. Therefore, the OC potential energy can be finally obtained as

$$W^{OC} = \Lambda^{cap^{-2}} W_K^{cap} + \Lambda^{oOV^{-2}} W_K^{oOV} - \oint_{its} B^{cap} (1+\nu) \kappa^{cap} \boldsymbol{q} \cdot \boldsymbol{m}_0 \ ds_0$$
 (S19)

where \oint_{its} denotes the contour integration along the intersection between the cap and oOV, and B^{cap} is an effective bending rigidity of the bi-layer cap region. It shows that the main contribution for the OC formation is a torque along the intersection between the cap and the oOV, associated with κ^{cap} .

Note that the effective bending rigidity B^{cap} can be estimated by projection of the 3D potential energy density onto the mid-surface for bi-layer shells. Utilizing the thickness ratio m and the moduli ratio n with the same notation as above, the potential energy of bi-layer shells can be expressed as

$$W^{bi} = \int \int_{h/2-h_1}^{h/2} \frac{E_2 n}{(1-\nu^2)} \Psi \ d\xi^3 da_0 + \int \int_{-h/2}^{-h/2+h_2} \frac{E_2}{(1-\nu^2)} \Psi \ d\xi^3 da_0$$
 (S20)

where Ψ is the 3D potential energy density. Meanwhile, the bi-layer shell's potential energy can be also expressed by using an effective Young's modulus E^{eff} as

$$W^{bi} = \int \int_{-h/2}^{h/2} \frac{E^{eff}}{(1 - \nu^2)} \Psi \ d\xi^3 da_0$$
 (S21)

in which equating (S20) and (S21) yields $E^{eff}=E_2(1+mn)/(1+m)$. Then, the effective Young's modulus of the cap E^{cap} can be estimated as $E_2\to E^{iOV}$ where E^{iOV} is the Young's modulus of the iOV, i.e. $E^{cap}=E^{iOV}(1+mn)/(1+m)$, which can be utilized to calculate $B^{cap}=\frac{E^{cap}h^3}{12(1-\nu^2)}$.

VI. ON THE EQUIVALENT SYSTEM OF THE OPTIC CUP AS AN OPEN SPHERICAL SHELL

In this letter, to analyze the elastic instabilities of OC morphogenesis, the entire OC is replaced with an equivalent system using an open spherical shell by treating the oOV as an effective rotational spring along the edge of the cap under the assumption that most of the oOV deformation occurs within its boundary layer as bending, as shown in Fig. (3) of the main text. This treatment physically means that the whole OC geometry consisting of the cap and the oOV is replaced by an open spherical shell, whose geometry is the same as the cap, with an equivalent edge torque whose magnitude is associated with the remaining value of κ^{cap} after overcoming the bending rigidity of the effective rotational spring. As a result, the natural quantity in the cap κ^{cap} relevant to the intersection torque of (S19) is equivalently transposed into κ^{eq} acting on a free-standing cap as written in Eq. (2) in the main text. In this section, we present the details of the derivation whereby we collect the entire OC potential energy into the cap region.

The OC potential energy W^{OC} of (S19) has two portions for the internal potential energy depending on deformations from the initial body in terms of the cap region (W_K^{cap}) and the oOV (W_K^{oOV}) . For the oOV deformation, it is reasonable to postulate that the oOV deformation mainly occurs within its boundary layer which is bending dominated [13]. As the width of the boundary layer is scaled as \sqrt{Rh} [10], the oOV colatitude-direction characteristic curvature in the boundary layer can be estimated using the angle change $\Delta\theta$ within the oOV boundary layer, i.e. $b_1^1 \sim \Delta\theta/\sqrt{Rh}$. Assuming the oOV colatitude-direction bending strain is much larger than the azimuthal one within the boundary layer, the oOV potential energy can be scaled as

$$\Lambda^{oOV^{-2}} W_K^{oOV} \sim \frac{B^{oOV}}{2} b_1^{1^2} A_{bl}^{oOV} \sim \pi \alpha B^{oOV} \Delta \theta^2 \sqrt{\frac{R}{h}}$$
 (S22)

where B^{oOV} is the oOV bending rigidity, and A_{bl}^{oOV} is the area of the oOV boundary layer region. As $\Delta\theta$ can be scaled as the change in the tangent angle at the intersection between the cap and the oOV, $\Delta\theta \sim \boldsymbol{q} \cdot \boldsymbol{m}_0$ with the rotation vector \boldsymbol{q} at the intersection [10]. Then, the OC potential energy can be collected into the cap region building on that the length of the intersection is $2\pi R\alpha$ for small α , as (S23) which represents a free-standing cap region with an equivalent edge torque,

$$W^{OC} = \Lambda^{cap^{-2}} W_K^{cap} - \oint_{ed} B^{cap} (1+\nu) \Delta \theta \left[\kappa^{cap} - \frac{B^{oOV}}{2B^{cap} (1+\nu)} \frac{\Delta \theta}{\sqrt{Rh}} \right] ds_0$$
 (S23)

where \oint_{ed} denotes the contour integration along the boundary edge of the free-standing cap region. That is, the whole OC is replaced by a free-standing cap with an equivalent edge torque associated with an equivalent natural curvature κ^{eq} that can be written as

$$\kappa^{eq} = \kappa^{cap} - \Gamma \frac{\Delta \theta}{\sqrt{Rh}} \tag{S24}$$

where $\Gamma = \frac{B^{oOV}}{2B^{cap}(1+\nu)}$, which coincides with Eq. (2) in the main text and is used to obtain the scaling laws for the critical natural curvature at the elastic instabilities governing OC formation as drawn on the phase diagrams of Fig. (4) in the main text.

VII. ON THE PRIMARY INVAGINATION VIA SNAP-THROUGH INSTABILITY

When a positive natural curvature is homogeneously imposed on an open spherical shell, the shell deforms to turn itself inside out. This eversion occurs via rapid, but smooth curvature change or rather sudden discontinuous displacement jump (i.e. snapping) depending on the shell geometry. Our numerical simulations of OC morphogenesis show that except for thicker shells, the primary invagination for most of the initial OC geometries occurs via the snap-through instability. Specifically, Fig. S3 shows that the apex displacement rate (dc/dt) of the OC in the insets is not constant during the two-step (primary and secondary) invagination as the snapping of the elastic shell proceeds with increasing speed [14], indicating that the phenomena we observe are snapping, and not rapid bending.

In this letter, the observation that the colatitude-direction tangent vector at the intersection between the cap and oOV becomes approximately horizontal, i.e. $\Delta\theta \approx \alpha$, at the primary invagination was used to get the scaling law for

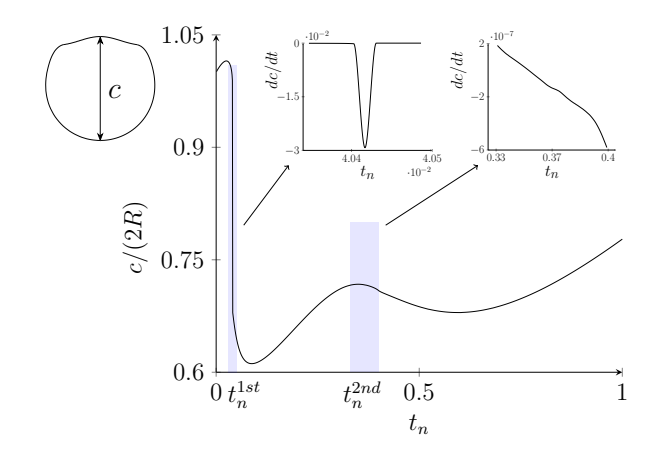


FIG. S3. The distance c from the apex to the bottom of the deforming OC with $\bar{\theta} = 2.21$ as a function of the normalized time. The inset shows the distance rate of the two-step invagination during the morphogenetic process of OC formation.

 $\kappa^{cap}R$ at the snapping instability point corresponding to Eq. (3) in the main text. In reality, the exact horizontal tangent vector is, however, only corresponding to the case where the shells are smoothly everted. So, in order to find the limit point $\bar{\theta}_s$ between the snapping and the smooth eversion, the minimum potential energy method is applied to the separated cap region that is a shallow shell. The displacement components on the deformed configuration can be obtained by minimizing (S14a) with the natural quantity set of the cap. Calculating the change in the tangent angle $\Delta\theta = \mathbf{q} \cdot \mathbf{m}_0$ with the obtained displacement at the boundary and equating it to α gives a value of natural curvature κ_h^{cap} which makes the tangent vector exactly horizontal as

$$\kappa_h^{cap} = \frac{10h^2 \left(\Lambda^2 (1+\nu) \left(\alpha^2 (1+\nu) + 9\right) - \alpha^2 (1+\nu)^2 - 9\nu - 3\right) + 3\alpha^2 \left(1-\Lambda^2\right) R^2 \left(1-\nu^2\right) \left(3\alpha^2 (1+\nu) + 20\right)}{2\Lambda^2 R (1+\nu) \left(5h^2 \left(\alpha^2 (1+\nu) + 6\right) - 3\alpha^4 R^2 \left(1-\nu^2\right)\right)}$$
(S25)

in which $\Delta\theta$ is calculated by using the stationary displacement components up to the fifth order for ξ^1 and the leading order for α .

Then, the fact that the tangent vector is not exactly horizontal for the snapping shell implies that the shells need an infinitely large κ_h^{cap} to make the tangent vector horizontal before the snapping, i.e. $1/\kappa_h^{cap} = 0$, and this hypothesis yields the transition point with $O(\alpha^2)$ as

$$\bar{\theta}_s = \left(\frac{10}{1 - \nu^2}\right)^{1/4} \tag{S26}$$

which is noted in the main text. This transition point $\bar{\theta}_s$ dictates the limit in initial geometry that separates smooth eversion and snap-through instability for the primary invagination.

VIII. ON CIRCULAR PLATE ANALYSIS

Due to the shallowness of the cap region of the OC, analyzing the symmetry-breaking buckling of bi-layer circular plates allows for a better understanding of the second instability phenomenon during OC morphogenesis. In this letter, the characteristic span and the buckling point of the bi-layer circular plate with the thickness-direction differential growth are utilized to analyze the secondary invagination and the symmetry-breaking buckling of the OC corresponding to Eq. (4-5) in the main text, and the detail of those derivations is dealt with in this section. Accordingly, the linear stability analysis is carried out in order to get an analytical equation for the critical natural curvature κ^p at the symmetry-breaking buckling of circular plates with radius R^p and thickness h, and the displacement solution obtained by the minimum potential energy method is applied for the characteristic span S^p of the deformed plate.

By following Koiter's work [16], a quadratic energy functional is obtained as

$$W_2[\hat{\boldsymbol{u}}; \Lambda, \kappa] = \int \frac{Y}{2} \left[\nu \varepsilon_{\alpha}^{\alpha} \varepsilon_{\gamma}^{\gamma} + (1 - \nu) \varepsilon_{\beta}^{\alpha} \varepsilon_{\alpha}^{\beta} \right] + \frac{B}{2} \left[\nu \varrho_{\alpha}^{\alpha} \varrho_{\gamma}^{\gamma} + (1 - \nu) \varrho_{\beta}^{\alpha} \varrho_{\alpha}^{\beta} \right] + \tau_{\sigma}^{\alpha\beta} \xi_{\alpha\beta} + \tau_{M}^{\alpha\beta} \zeta_{\alpha\beta} \ da_0$$
 (S27)

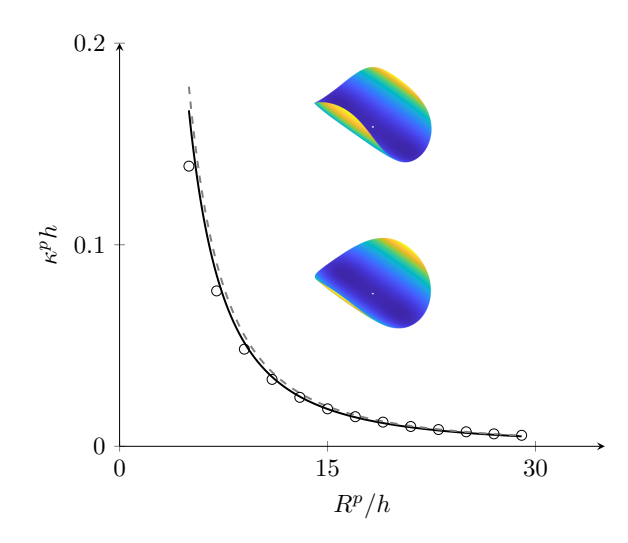


FIG. S4. The symmetry-breaking buckling natural curvature for circular plates with different R^p/h . The solid line is the analytical equation of (S35) while the dashed line is the one proposed in [15]. The circles denote numerical simulation results at m = 1/9, n = 50, and $\nu = 0.45$ corresponding the OC properties.

where \hat{u} is the displacement vector from the fundamental (equilibrium) configuration, and $\varepsilon_{\alpha\beta}$ and $\varrho_{\alpha\beta}$ are the linear membrane and bending strains with respect to the fundamental configuration, and $\xi_{\alpha\beta}$ and $\zeta_{\alpha\beta}$ are the nonlinear second-order membrane and bending strains with respect to the fundamental configuration.

Building on the fact that ξ^1 and ξ^2 are respectively the radial and polar coordinates, the displacement component on the fundamental configuration can be obtained by minimizing (S14a) and inserting the plate's natural quantity set, i.e. $\{\Lambda^p, \kappa^p\}$, and $R \to \infty$ under the axisymmetry condition as

$$u_1^s = -\frac{1}{2}(1+\nu)\xi^1(1-\Lambda^{p^2}) \; ; \quad u_2^s = 0$$
 (S28a)

$$w^{s} = \frac{1}{2}(1+\nu)\xi^{1^{2}}\kappa^{p}\Lambda^{p^{2}}$$
 (S28b)

where u_{α}^{s} and w^{s} are the solutions of the displacement components on the fundamental configuration as $\boldsymbol{u}^{s} = u_{\alpha}^{s} \boldsymbol{a}^{\alpha} + w^{s} \boldsymbol{n}_{0}$ with the initial dual vector \boldsymbol{a}^{α} . Then, this gives the membrane and bending stresses caused by the natural stretching and curvature as

$$\tau_{\sigma}^{22} = \frac{Y\left(1 - \Lambda^{p^2}\right)\left(1 - \nu^2\right)}{2\Lambda^{p^4}\xi^{1^2}}; \quad \tau_{\sigma}^{11} = \tau_{\sigma}^{12} = \tau_{\sigma}^{21} = 0$$
 (S29a)

$$\tau_M^{22} = -\frac{B\kappa^p \left(1 - \nu^2\right)}{\Lambda^{p^2} \xi^{1^2}}; \quad \tau_M^{11} = \tau_M^{12} = \tau_M^{21} = 0$$
 (S29b)

In this section, it is assumed that the components of \hat{u} have forms based on the first term of a Fourier series as

$$\hat{u}_1 = Cu_1^s \sin(n_1 \xi^2) = -\frac{1}{2}C(1+\nu)\xi^1(1-\Lambda^{p^2})\sin(n_1 \xi^2)$$
(S30a)

$$\hat{u}_2 = Cu_2^s \sin(n_2 \xi^2) = 0 \tag{S30b}$$

$$\hat{w} = Cw^s \sin(n_3 \xi^2) = \frac{1}{2} C(1+\nu) \xi^{1^2} \kappa^p \Lambda^{p^2} \sin(n_3 \xi^2)$$
 (S30c)

where C is a constant real number, and n_1 , n_2 , and n_3 are integer numbers.

Then, with the small deformation assumption, the Donnell-Mushtari-Vlasov theory gives the linear and nonlinear second-order strains [10], as

$$\varepsilon_{\alpha\beta} = \frac{1}{2} (\nabla_{\alpha} \hat{u}_{\beta} + \nabla_{\beta} \hat{u}_{\alpha}) - \mathring{b}_{\alpha\beta} \hat{w}$$
 (S31a)

$$\varrho_{\alpha\beta} = \nabla_{\alpha} \nabla_{\beta} \hat{w}, \tag{S31b}$$

$$\xi_{\alpha\beta} = \frac{1}{2} \nabla_{\alpha} \hat{w} \nabla_{\beta} \hat{w} \tag{S32a}$$

$$\zeta_{\alpha\beta} = \nabla^{\gamma} \hat{u}_{\gamma} \nabla_{\beta} \nabla_{\alpha} \hat{w} - \nabla^{\gamma} \hat{w} \nabla_{\beta} \nabla_{\alpha} \hat{u}_{\gamma} \tag{S32b}$$

such that the resulting balance equation obtained via the first variation of (S27) with the integration domain $\xi^1:[0,R^p]$ and $\xi^2:[0,\pi/2]$ leads to the critical natural curvature including Λ^p at the symmetry-breaking buckling as

$$\kappa^{p^{2}} = \frac{2\left(1 - \Lambda^{p^{2}}\right)\left(4(\nu + 1)\sin\left(\pi n_{1}\right) + n_{1}\left((\nu - 1)n_{1}\left(\pi n_{1} + \sin\left(\pi n_{1}\right)\right) - 4\pi(\nu + 1)\right)\right)}{R^{p^{2}}\Lambda^{p^{4}}\left(1 - \nu^{2}\right)n_{1}n_{3}\left(\pi n_{3} + \sin\left(\pi n_{3}\right)\right)}$$
(S33)

which is obtained by Taylor expanding κ^{p^2} up to the first order in h.

Since the natural stretching Λ^p and curvature κ^p are both functions of the differential growth characteristics on each layer of the bi-layer surface, for the case where the upper layer is passive (i.e. $e_1 = 1$) like the cap region of the OC, solving (S17) and (S18) with respect to e_2 up to the first order and equating those to each other gives a relation equation as

$$\Lambda^{p^2} = \frac{h\kappa^p (1 + m(3n - 2))}{3mn} + 1 \tag{S34}$$

which yields the normalized critical natural curvature in the main text, not including Λ^p , with $n_1 = 1$ and $n_3 = 2$ to make it minimum as

$$\kappa^p h = \pm \chi \frac{(5+3\nu)}{(1-\nu^2)} \left(\frac{h}{R^p}\right)^2. \tag{S35}$$

where $\chi = (1 + m(3n - 2))/(6mn)$. This analytical equation was utilized to estimate the critical natural curvature at the symmetry-breaking buckling for open spherical shallow shells by using $R^p \to R\alpha$ for large radius R and small opening angle α , which is extended to Eq. (5) in the main text.

In addition, using (S28a) and (S34) gives the characteristic span of the deformed circular plate with $\xi^1 = R^p$ as

$$S^p = R^p \left(1 + \chi (1 + \nu) h \kappa^p \right) \tag{S36}$$

This length can be generalized to the span of open spherical shallow shells by using $R^p \to R\alpha$, which implies that the characteristic span of the cap region of the OC will scale as $S^{cap} \sim R\alpha(1+\chi(1+\nu)h\kappa^{cap})$ that is utilized to estimate the secondary invagination point of Eq. (4) in the main text.

Note that our analytical equation for the critical $\kappa^p h$ gives similar results with the one proposed via an energy comparison approach in [15] as $\kappa^p h = \pm \sqrt{10 + 7\sqrt{2}(h/R^p)^2}$, and is well-matched with the numerical simulation results for the symmetry-breaking buckling of bi-layer circular plates with different R^p/h as shown in Fig. S4.

IX. THE SCALING OF $\Delta\theta$ AT THE SYMMETRY-BREAKING BUCKLING INSTABILITY

In the main text, the angle change $\Delta\theta$ along the oOV boundary layer at the symmetry-breaking buckling instability is scaled as $\sqrt{R/h}$ of Eq. (6) in the main text. In this section, this scaling is derived. When an open spherical shell is under an edge torque M_{edge} , we can write its shell energy using the assumption that the deformation mainly occurs within its boundary layer and is bending dominated, i.e. $b_1^1 \sim \Delta\theta/\sqrt{Rh}$ [13], as

$$W \sim \frac{B}{2}b_1^{1^2}A_{bl} - \oint M_{edge}\Delta\theta \ ds_0 \sim \pi\alpha B\Delta\theta^2 \sqrt{\frac{R}{h}} - 2\pi R\alpha M_{edge}\Delta\theta. \tag{S37}$$

where A_{bl} is the area of the boundary layer region in the open spherical shell. Then, the minimum potential energy $\frac{dW}{d\Delta\theta} = 0$ yields $\Delta\theta \sim M_{edge}\sqrt{Rh}/B$. If natural curvature are the origin of the edge torque, $M_{edge} \sim B\kappa$ can be used according to (S15). Then, since $\kappa \sim 1/h$ based on (S18), $\Delta\theta \sim \sqrt{R/h}$ is obtained.

X. THE EFFECT OF DIFFERENT MATERIAL PROPERTIES

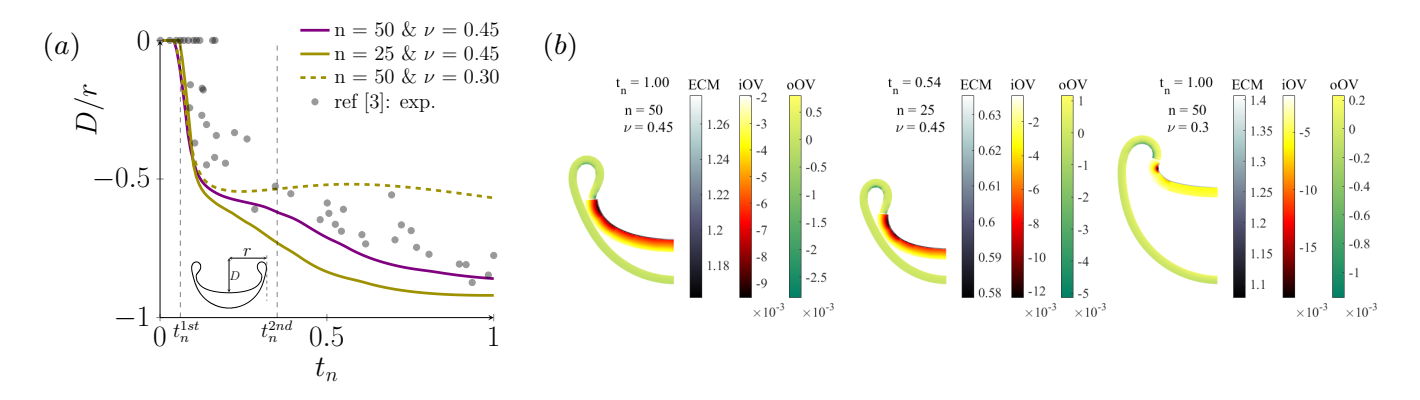


FIG. S5. (a) The OC invagination depth change with different material properties, the moduli ratio n and the Poisson ratio ν . (b) Normalized residual stress contour for the colatitude-direction component as $10^{-10}\Sigma^{11}/E^{iOV}$.

The analysis for OC morphogenesis in the main text focused on the effects of the initial OC geometry with material properties chosen following previous experimental studies [3, 5, 17], modeling the eye tissue as a compressible elastic material [18, 19]. Here, we present the results of numerical simulations where different material properties were considered to examine their effects on OC morphogenesis.

For $\bar{\theta}=1.56$ with $\alpha=40^\circ$ and accounting for mass changes, various values of the shear modulus of the ECM were considered by varying the moduli ratio $n=\mu^{ECM}/\mu^{iOV}$ as well as different Poisson's ratios ν , noting that the OVs shear modulus $\mu^{iOV}=\mu^{oOV}=220\mathrm{Pa}$. As shown in Fig. S5(a), the invagination depth of the OC is affected by both the moduli ratio and the Poisson's ratio as the larger moduli ratio and the smaller Poisson's ratio result in a shallower depth. Fig. S5(b) shows the residual stresses in the ECM, iOV, and oOV for different material properties and invagination depths. These snapshots show that, in general, the residual stresses are larger and more widely distributed for deeper invagination depths. This residual stress contour, in which the growing iOV and oOV are in compression whereas the passive ECM is in tension, follows the general trend of residual stresses induced by growth as growing bodies involve compressive stresses for local, differential growth cases [7]. Furthermore, in contrast to the cup shape formation through invagination, in good agreement with prior work [3] OC formation fails for $n \leq 10$, as the contribution of the ECM constraint becomes too small, resulting in evagination, as shown in Fig. S6(a).

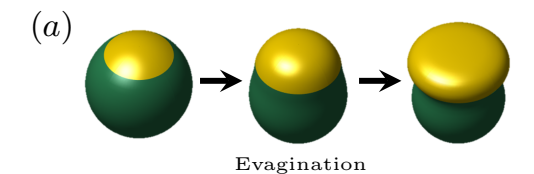
Additionally, as our computational model for OC formation is performed based on the nonlinear, compressible neo-Hookean constitutive model, we investigated the effect of Poisson's ratio on the critical natural curvature at the second instability points for thick ($\bar{\theta} = 1.85$) and thin ($\bar{\theta} = 3.04$) shells with $\alpha = 40^{\circ}$ within the biologically-relevant range of $0.4 \le \nu \le 0.49$ for eye tissues [18, 19], including incompressible limit of $\nu = 0.5$ with a constraint $J_m = 1$. As a result, the secondary invagination and the symmetry-breaking buckling occurred regardless of the Poisson's ratio for the thick and thin shells, respectively, as shown in Fig. S6(b). This indicates that material compressibility is not required for the secondary invagination and symmetry-breaking buckling to occur during OC morphogenesis. Furthermore, the simulation results in Fig. S6(b) show that Poisson's ratio merely shifts the critical natural curvature for both secondary invagination and symmetry-breaking buckling to occur. Based on these results, for the main text we chose the previously experimentally-reported value of 0.45 for the Poisson's ratio, and focused on the effect of initial geometries on the critical natural curvature to analyze the instability-induced OC morphogenesis via our scaling laws of Eq. (3,5-6) and Fig. (4) in the main text.

^[1] R. A. Sauer and T. X. Duong, On the theoretical foundations of thin solid and liquid shells, Mathematics and mechanics of solids 22, 343 (2017).

^[2] F. Roohbakhshan and R. A. Sauer, Efficient isogeometric thin shell formulations for soft biological materials, Biomechanics and modeling in mechanobiology 16, 1569 (2017).

^[3] A. Oltean, J. Huang, D. C. Beebe, and L. A. Taber, Tissue growth constrained by extracellular matrix drives invagination during optic cup morphogenesis, Biomechanics and modeling in mechanobiology 15, 1405 (2016).

^[4] A. G. Holzapfel, Nonlinear solid mechanics ii, (2000).



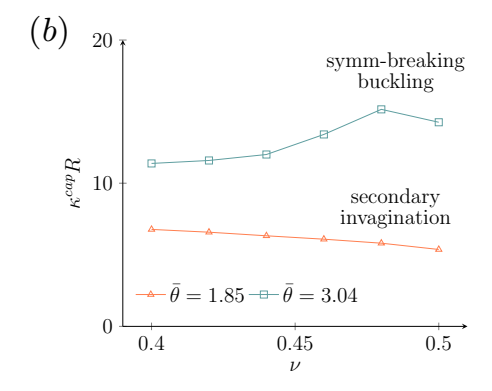


FIG. S6. (a) Failure of the OC formation through the evagination for n=10 and $\nu=0.45$. (b) Critical natural curvature at the second instabilities (secondary invagination and symmetry-breaking buckling), depending on Poisson's ratio for thick $(\bar{\theta}=1.85)$ and thin $(\bar{\theta}=3.04)$ shells with $\alpha=40^{\circ}$.

- [5] H. S. Hosseini and L. A. Taber, How mechanical forces shape the developing eye, Progress in biophysics and molecular biology 137, 25 (2018).
- [6] M. Ben Amar and A. Goriely, Growth and instability in elastic tissues, Journal of the Mechanics and Physics of Solids 53, 2284 (2005).
- [7] A. Goriely, The mathematics and mechanics of biological growth, Vol. 45 (Springer, 2017).
- [8] E. Efrati, E. Sharon, and R. Kupferman, Elastic theory of unconstrained non-euclidean plates, Journal of the Mechanics and Physics of Solids 57, 762 (2009).
- [9] W. T. Koiter and J. G. Simmonds, Foundations of shell theory, in *Theoretical and applied mechanics* (Springer, 1973) pp. 150-176.
- [10] F. I. Niordson, Shell theory (Elsevier, 2012).
- [11] M. Pezzulla, N. Stoop, X. Jiang, and D. P. Holmes, Curvature-driven morphing of non-euclidean shells, Proceedings of the Royal Society A: Mathematical, Physical and Engineering Sciences 473, 20170087 (2017).
- [12] A. Lucantonio, P. Nardinocchi, and M. Pezzulla, Swelling-induced and controlled curving in layered gel beams, Proceedings of the Royal Society A: Mathematical, Physical and Engineering Sciences 470, 20140467 (2014).
- [13] E. Efrati, E. Sharon, and R. Kupferman, Buckling transition and boundary layer in non-euclidean plates, Physical Review E 80, 016602 (2009).
- [14] S. Höhn, A. R. Honerkamp-Smith, P. A. Haas, P. K. Trong, and R. E. Goldstein, Dynamics of a volvox embryo turning itself inside out, Physical review letters 114, 178101 (2015).
- [15] M. Pezzulla, G. P. Smith, P. Nardinocchi, and D. P. Holmes, Geometry and mechanics of thin growing bilayers, Soft Matter 12, 4435 (2016).
- [16] W. T. Koiter and A. Van Der Heijden, WT Koiter's elastic stability of solids and structures (Cambridge University Press Cambridge, UK; New York, NY, USA, 2009).
- [17] G. Xu, P. S. Kemp, J. A. Hwu, A. M. Beagley, P. V. Bayly, and L. A. Taber, Opening angles and material properties of the early embryonic chick brain, Journal of biomechanical engineering 132 (2010).
- [18] E. Uchio, S. Ohno, J. Kudoh, K. Aoki, and L. T. Kisielewicz, Simulation model of an eyeball based on finite element analysis on a supercomputer, British Journal of Ophthalmology 83, 1106 (1999).
- [19] I. A. Sigal, J. G. Flanagan, and C. R. Ethier, Factors influencing optic nerve head biomechanics, Investigative ophthalmology & visual science 46, 4189 (2005).